Enhanced visible-light-driven reduction of hexavalent chromium under neutral conditions using quasi-MOF photocatalysts via thiocyanate modulation

Yi ZHANG[1#], Han-xiao LIAO[2#], Lu YANG[3], Bin-hua ZHOU[1], Xuan-zhi LIU[1], Huan-huan ZHAI[1], Xiao-rong HE[1], Hong-jun HUANG[4], Peng-fei TAN[1], Jun PAN[1]

1. State Key Laboratory of Powder Metallurgy, Central South University, Changsha 410083, China;
2. School of Metallurgy and Environment, Central South University, Changsha 410083, China;
3. Hunan Province Key Laboratory of Applied Environmental Photocatalysis, Changsha University, Changsha 410022, China;
4. School of Minerals Processing and Bioengineering, Central South University, Changsha 410083, China

Abstract: In order to address the issue that the photocatalytic reduction of hexavalent chromium (Cr(VI)) is often limited by the inefficient utilization of electrons in photocatalysts, a quasi-MOF photocatalyst using thiocyanate (—SCN) was developed as a modulator to enhance the charge transfer properties of ZIF-L-based photocatalysts. The incorporation of —SCN introduced structural defects, which improved visible light absorption and the reduction ability of photogenerated electrons. —SCN significantly adjusted the electronic properties and established a stable electron release pathway, serving as active sites for reduction. The optimized quasi-MOF demonstrated a Cr(VI) reduction rate of 94.8% in neutral potassium thiocyanate solution under visible light without a hole scavenger. The reaction rate constant is 2.8 times that of the photocatalyst without defect modulation. This study offers a promising strategy for developing highly efficient photocatalysts for environmental remediation.

Key words: quasi-MOF; polar ligand; photocatalysis; hexavalent chromium reduction

1 Introduction

Photocatalytic reduction of Cr(VI) represents an effective approach for mitigating Cr(VI) pollution in water [1,2]. In industrial settings, chromium-containing wastewater often presents neutral to weakly alkaline conditions, as observed in the tanning industry [3]. However, most photocatalysts for Cr(VI) reduction are currently developed under acidic conditions favorable for the catalytic process, exhibiting reduced activity under non-acidic conditions. As the pH increases, the thermodynamic driving force for Cr(VI) reduction theoretically decreases by 79 mV/pH unit [4]. In addition, the utilization of photogenerated electrons by Cr(VI) through various pathways directly determines the reduction activity of the photocatalyst [5,6]. Therefore, the development in Cr(VI) reduction photocatalysis with improved electronic utilization in non-acidic conditions is of paramount significance.

# Yi ZHANG and Han-xiao LIAO contributed equally to this work
Corresponding author: Jun PAN, Tel: +86-18273184694, E-mail: jun.pan@csu.edu.cn;
      Peng-fei TAN, Tel: +86-13017287406, E-mail: tpf0203@csu.edu.cn;
      Hong-jun HUANG, Tel: +86-13787020194, E-mail: peacehhj@126.com

Besides the heterojunction strategy, the defect engineering in MOF photocatalysts has a huge impact on the material morphology, electronic structure, and photocatalytic performance [7−9]. Defects in the photocatalysts are advantageous for enhancing the visible-light response [10]. The introduction of modulators has been reported as an effective strategy to enhance photocatalytic activity by constructing quasi-MOFs with a substantial number of structural defects [7,11]. For example, ZHANG et al [12] improved the photocatalytic performance of ZIF-67 by replacing some original ligands through competitive coordination with vanillin. However, the majority of currently employed modulators primarily contribute to structural regulation and have little impact on the charge migration process of the quasi-MOFs.

Thiocyano- (—SCN), as a polar functional group, exhibits a strong affinity for metal sites and a robust electron drawing ability. This property allows it to construct a stable transmission channel for photogenerated electrons of the MOFs and serve as an active reaction site, promoting the reduction process [13]. Due to its strong nucleophilicity, the sulfur atom in thiocyanate can be regarded as an active catalytic site at the interface, enhancing the transfer rate of photogenerated electrons at the interface [14]. Therefore, it is advantageous for promoting the reduction of Cr(VI) under non-acidic conditions from a kinetic perspective. Currently, there are reports only on utilizing the electron-withdrawing properties of —SCN to modulate the charge transfer behavior of TiO_2 and metal nanoparticles [14−16]. This approach has not yet been applied in MOF-based photocatalytic materials. Considering the facile modifiability of MOF structures, —SCN holds promising potential as an effective group for constructing and regulating quasi-MOFs photocatalysts [17].

To enhance the non-acidic photocatalytic activity of ZIFs-based photocatalysts, this work employed KSCN as a modulator to introduce —SCN into the previously reported Fe—O clusters-sensitized ZIF-L, leading to the construction of a quasi-MOF structure. XPS, FT-IR, Raman, and other analyses confirmed the introduction of — SCN and the formation of the quasi-MOFs structure. Photo/electrochemical experiments were conducted to elucidate the charge transfer properties of samples, demonstrating the notable influence of —SCN introduction on the migration of photo-generated carriers during the photocatalytic process. This study provides a new way for the synthesis of quasi-MOF photocatalysts via thiocyanate modulation, which subsequently achieved efficient non-acidic reduction of Cr(VI).

2 Experimental

2.1 Materials

Iron nitrate nonahydrate ($Fe(NO_3)_3 \cdot 9H_2O$, AR), mannitol ($C_6H_{14}O_6$, AR), potassium dichromate ($K_2Cr_2O_7$, AR), potassium thiocyanate (KSCN, AR), methanol (MeOH, CH_3OH, AR), potassium hydroxide (KOH, AR), isopropanol (IPA, C_3H_8O), glycol ($C_2H_6O_2$, AR), acetone (C_3H_6O, AR), and sulfuric acid (H_2SO_4, GR) were supplied by Sinopharm Chemical Reagent Co., Ltd. 2-methyl-imidazole ($C_4H_6N_2$, 98%) and 1,5-diphenylcarbazide ($C_{13}H_{14}N_4O$, AR) were supplied by Aladdin Reagent Co., Ltd. Zinc nitrate hexahydrate ($Zn(NO_3)_2 \cdot 6H_2O$, AR), sodium sulfate (Na_2SO_4, AR), and phosphoric acid (H_3PO_4, GR) were supplied by Xilong Scientific Co., Ltd. The above reagents were not further purified.

2.2 Characterizations

Scanning electron microscope (SEM) images, X-ray diffraction patterns (XRD), Fourier transform infrared spectroscopy (FT-IR) and Raman spectra were obtained via Helios Nanolab G3 UC electron microscope, Bruker D8 Advance diffractometer, Nicolet iS20 spectrometer, and LabRAM Aramis spectrometer, respectively. Transmission electron microscope (TEM) images and energy spectrum data were obtained on JEM-F200. The PerkinElmer STA 8000 simultaneous thermal analyzer was used to test the structure of MOFs via differential scanning calorimetry and thermogravimetric analysis (DSC−TGA). The electron paramagnetic resonance (EPR) spectra were obtained by Bruker EMXplus-6/1 spectrometer to determine the structural defects of the materials. The water contact angle obtained by Kruss DSA100 contact angle measuring instrument was used to determine the change of hydrophilicity and surface energy of the MOFs. The X-ray photoelectron spectroscopy (XPS) results were recorded on ESCALAB Xi+ spectrometer. Diffuse reflectance spectra (DRS) of the as-synthesized MOFs were measured on Evolution

220 spectrophotometer. The photoluminescence (PL) experiments were performed at an F97Pro fluorospectro photometer. Transient photoluminescence (TR-PL) experiments were performed at an Edinburgh FLS1000 fluorospectro photometer. The Mott−Schottky measurements, transient photocurrent response, electrochemical impedance spectroscopy (EIS), circulation voltammetry (CV) and linear sweep voltammetry (LSV) curves were conducted on the CHI660E electrochemical workstation.

2.3 Synthesis of FZ sample

This preparation method is slightly modified from the previously reported procedure (as shown in Scheme 1(a)) [18]. 2 mmol $Zn(NO_3)_2·6H_2O$ and 0.5 mmol $Fe(NO_3)_3·9H_2O$ were added into a beaker filled with 40 mL deionized water and stirred until fully dissolved. Subsequently, 5 mmol of mannitol was added to the solution and stirred for 30 min. Then, 20 mL of 2-methylimidazole aqueous solution (0.8 mol/L) was added dropwise to the beaker. The mixture was stirred at room temperature for 24 h. The obtained suspension was centrifuged to collect the precipitate, washed several times by alternating centrifugation with deionized water and ethanol, and finally dried in a vacuum oven at 60 °C overnight. This sample was labeled as FZ in subsequent experiments.

2.4 Synthesis of xS-FZ sample

The synthesis process is shown in Scheme 1(b). 2 mmol $Zn(NO_3)_2·6H_2O$ and 0.5 mmol $Fe(NO_3)_3·9H_2O$ were added into a beaker filled with 40 mL deionized water and stirred until fully dissolved. Following that, 5 mmol of mannitol and a specific quantity of KSCN were introduced into the beaker, and the mixture was stirred for 30 min. 20 mL of 2-methylimidazole aqueous solution (0.8 mol/L) was added dropwise to the beaker. The mixture was stirred at room temperature for 24 h. The resultant mixture was stirred at room temperature for 24 h. The resulting suspension was subjected to centrifugation to gather the precipitate, which underwent several wash cycles through alternating centrifugation with deionized water and ethanol. Subsequently, the collected material was dried in a vacuum oven at 60 °C overnight. Each resulting sample was denoted as xS-FZ (where x means the amount of KSCN, i.e., x=0.2, 0.5, 1 mmol) for subsequent experiments.

2.5 Photocatalytic experiments

The photocatalytic properties of the as-synthesized photocatalysts were characterized by Cr(VI) reduction experiments using a Microsolar
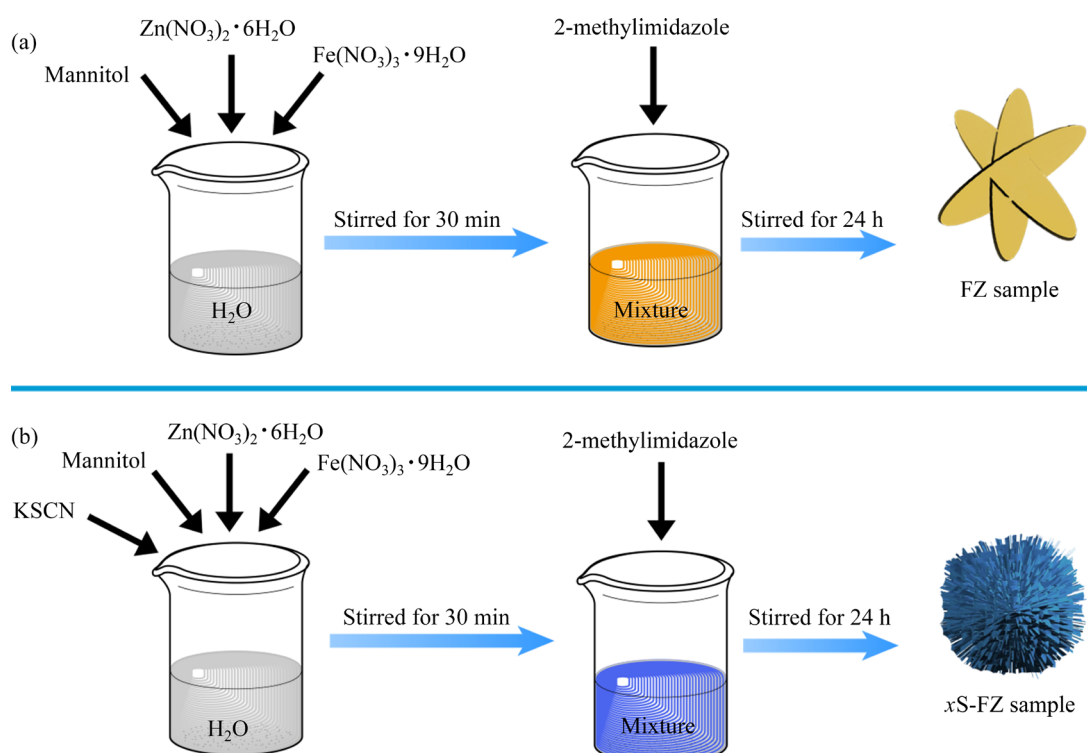
Scheme 1 One-step synthesis diagram of FZ (a) and xS-FZ (b) samples

300 Xenon lamp (light intensity 100 mW/cm², device rated power 300 W, 420 nm cutoff filter installed) positioned 10 cm away from the liquid surface. In a typical procedure, 100 mL of $K_2Cr_2O_7$ solution (30 mg/L, adjusted to a pH of 7) was ultrasonicated with 50 mg of the photocatalyst. For 30 min in the dark, the mixture was stirred to attain adsorption−desorption equilibrium. After equilibrium, the photocatalytic reaction was performed under illumination, and samples were taken at 15 min interval. The Cr(VI) contents of samples were determined by the 1,5-diphenyl-carbazide (DPC) colorimetric method with an Evolution 220 spectrophotometer at 540 nm.

In this test, the apparent rate constant (k) was applied to describing the reduction kinetics of Cr(VI):

$$k = \frac{\ln(C_0/C_t)}{t} \tag{1}$$

where C_0 and C_t represent the Cr(VI) concentrations before and after the photocatalytic reaction, correspondingly. t is the total time of photocatalytic Cr(VI) reduction.

3 Result and discussion

3.1 Characterizations of MOFs

The XRD patterns of as-synthesized samples were depicted in Fig. 1(a). According to previous reports, the composition of Fe—O clusters into ZIF-L in the form of mannitol−Fe complex does not damage the phase and crystallinity of ZIF-L [18]. Each diffraction peak of the xS-FZ samples was corresponded well to the XRD pattern simulated by the CIF file (CCDC-1509273) of ZIF-L, indicating that the addition of KSCN during the synthesis process did not completely disrupt the framework structure of ZIF-L. Theoretically, the substitution of —SCN for ligands in ZIF-L results in an increase in the number of structural defects. The progressive decline in the intensity of characteristic peaks was associated with the gradual increase in the number of —SCN ligand replacements in ZIF-L, corresponding to the reduction in the crystallinity of the materials [19].
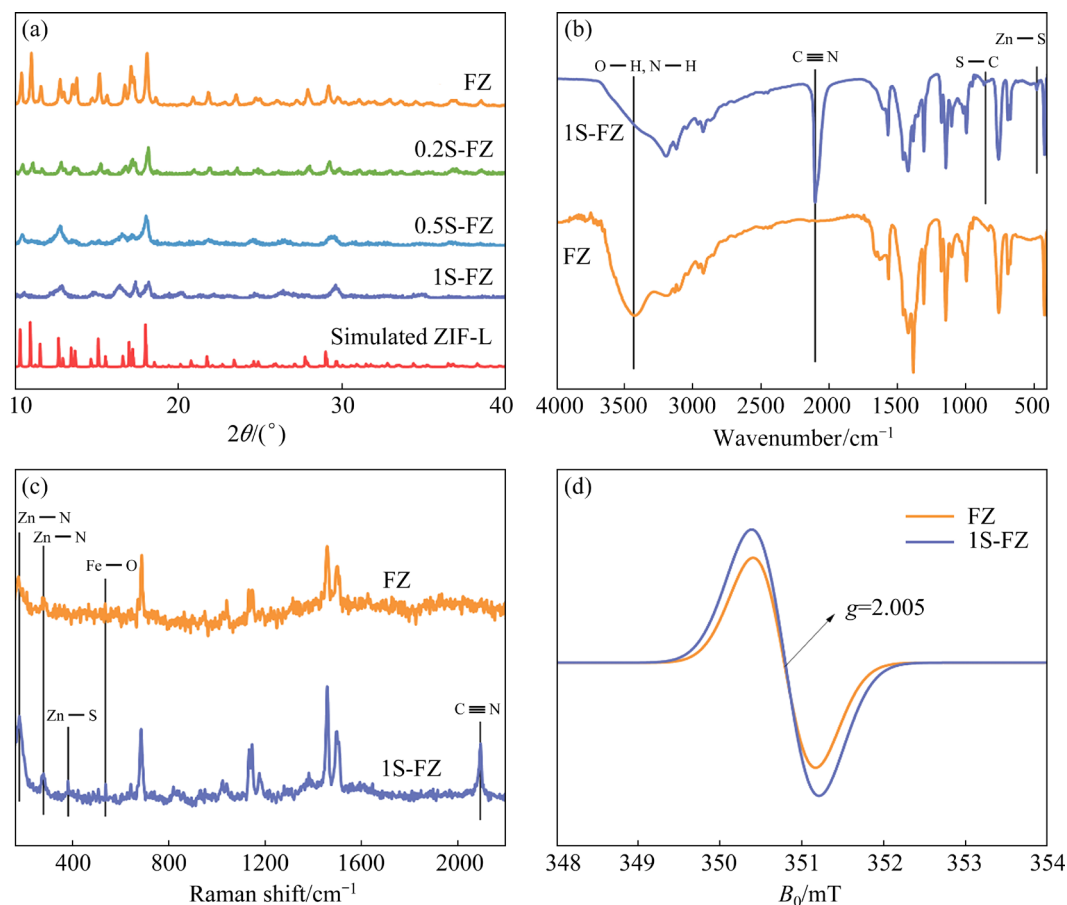

Fig. 1 XRD patterns (a), FT-IR spectra (b), Raman spectra (c), and EPR spectra (d) of as-synthesized samples

To confirm the introduction of ─SCN in the samples, the chemical structure was characterized through FT-IR and Raman spectroscopy. The results were presented in Figs. 1(b, c). Both FZ and 1S-FZ sample exhibit good correspondence with the chemical structure of ZIF-L [20]. In the FT-IR spectrum of 1S-FZ, the characteristic peaks corresponding to stretching vibrations of S─C (866 cm^{-1}) and C≡N (2104 cm^{-1}) were observed, indicating the existence of ─SCN [21]. In addition, the stretching vibration peak of Zn─S was observed at 479 cm^{-1} [22]. The Raman spectrum of 1S-FZ clearly showed the retention of Zn─N (179 and 275 cm^{-1}) and Fe─O (538 cm^{-1}) stretching vibrations in the Fe─O clusters@ZIF-L structure [23,24]. The characteristic peak of the Zn─S (382 cm^{-1}), and C≡N (2095 cm^{-1}) could also be observed [25]. These results confirm that ─SCN primarily coordinated with Zn sites in the composite material without disrupting the composite structure of the Fe─O clusters@ZIF-L. Moreover, a notable reduction in the intensity of hydrogen bonding stretching vibrations (around 3420 cm^{-1}) in the FT-IR spectrum of 1S-FZ was observed, attributed to the substitution of partial monodentate 2-methylimidazole ligand of ZIF-L by ─SCN, resulting in a decrease in the strength of hydrogen bonding [26]. In the EPR spectra, it can be seen that the original structural defect signal from the removal of solvent molecules was enhanced (Fig. 1(d)). As ─SCN coordinates with Zn, replacing the original bidentate 2-methyl-imidazole ligand, it inevitably introduces more structural defects [12].

As shown in Fig. 2, SEM was employed to characterize the morphological changes of the photocatalytic material before and after modification. The FZ sample exhibited growth with multiple crystal plane orientations while maintaining the elliptical nanosheet morphology, resulting in a cross-shaped appearance. This phenomenon is primarily attributed to the constraints imposed by the surface energy of ZIF-L [27,28]. With an increasing amount of added KSCN, the particle size of 0.2S-FZ sample became smaller, and the shape became more irregular and fragmented. The 0.5S-FZ and 1S-FZ samples were transformed into needle-like particles and self-
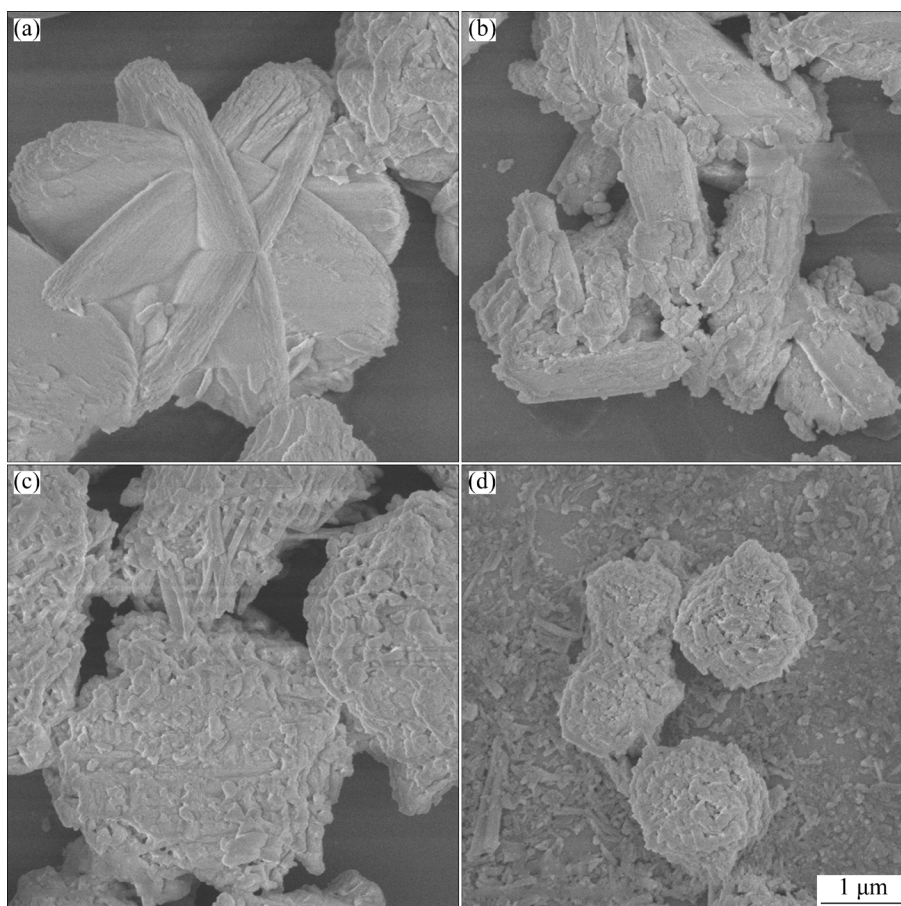

Fig. 2 SEM images of FZ (a), 0.2S-FZ (b), 0.5S-FZ (c) and 1S-FZ (d) samples

assembled into micron-sized balls. In Fig. 3(a), the TEM image of the 1S-FZ sample was presented. It was revealed that the 1S-FZ sample was assembled from numerous nanorods with a width of 50 nm approximately. This altered morphology was more conducive to the degradation process of Cr(VI) on the surface of the photocatalyst. Through EDS mapping scanning analysis in Figs. 3(b−h), it was evident that S, N, O, Fe, Zn, and C were uniformly distributed, underscoring successful introduction of —SCN.

Figure 4 presents XPS spectra of FZ and 1S-FZ samples. In the 1S-FZ sample, the characteristic peaks of sulfur appeared, and the —SCN peak could be identified at 399.1 eV, providing evidence of introduction of —SCN [16].

With the introduction of —SCN, characteristic peaks of Zn shifted towards higher binding energy, indicating the decrease in the electron cloud density of Zn [29]. This is primarily attributed to the electron-withdrawing effect of —SCN, which promotes the generation of an intrinsic electric field [30−32]. In comparison to Zn 2p, the shift in the characteristic peaks of Fe 2p was relatively minimal, indicating the effective protection of Fe sites by the strong chelating action of mannitol. In addition, Thiocyanate ion is an asymmetric ion with interfacial dipole moment on the surface of the material. Controlling the surface potential by introducing a dipole effect can improve the electron transfer dynamics [15]. With the addition of KSCN, zeta potential of MOFs changed from −8.0 to
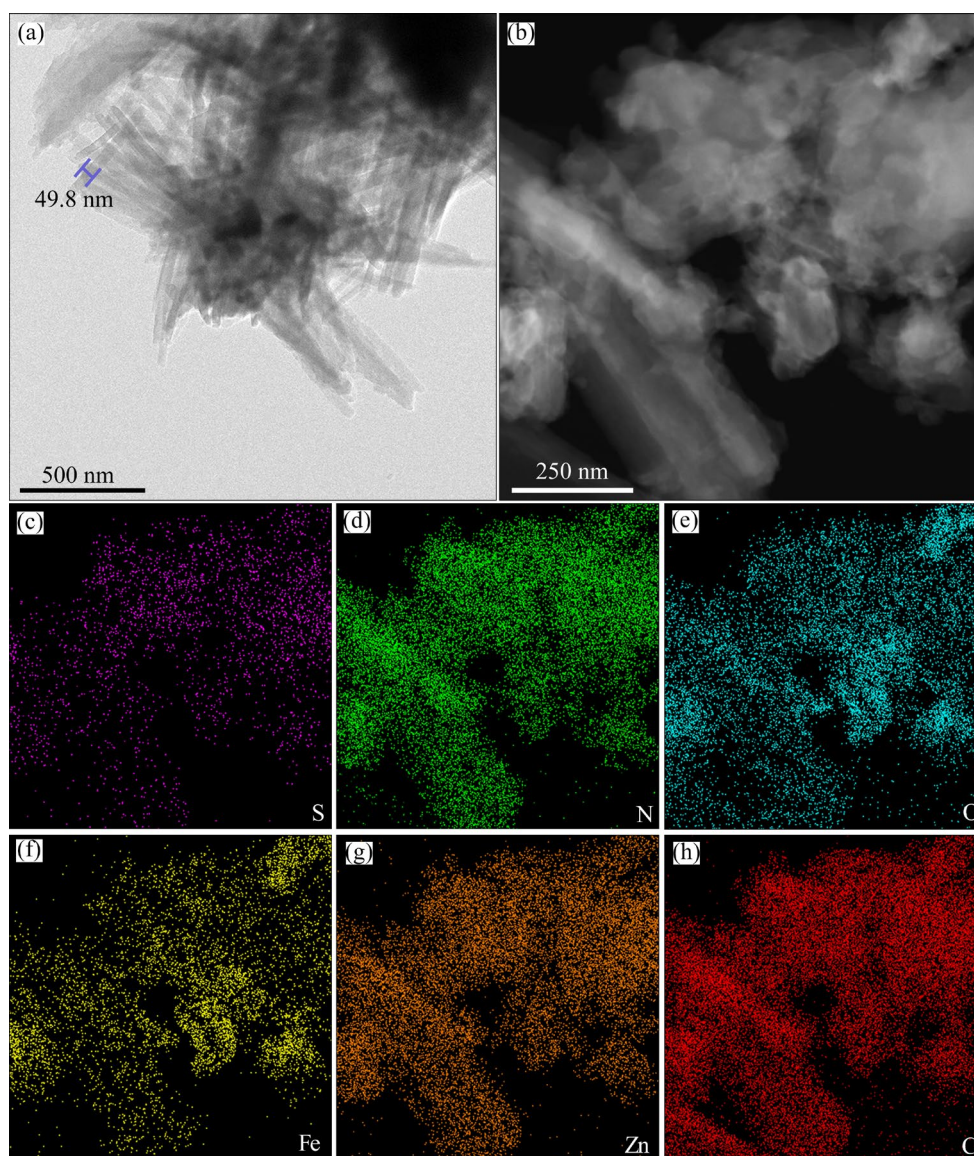
Fig. 3 TEM image (a), STEM-HADDF image (b) and corresponding element mapping images of S (c), N (d), O (e), Fe (f), Zn (g) and C (h) of 1S-FZ sample
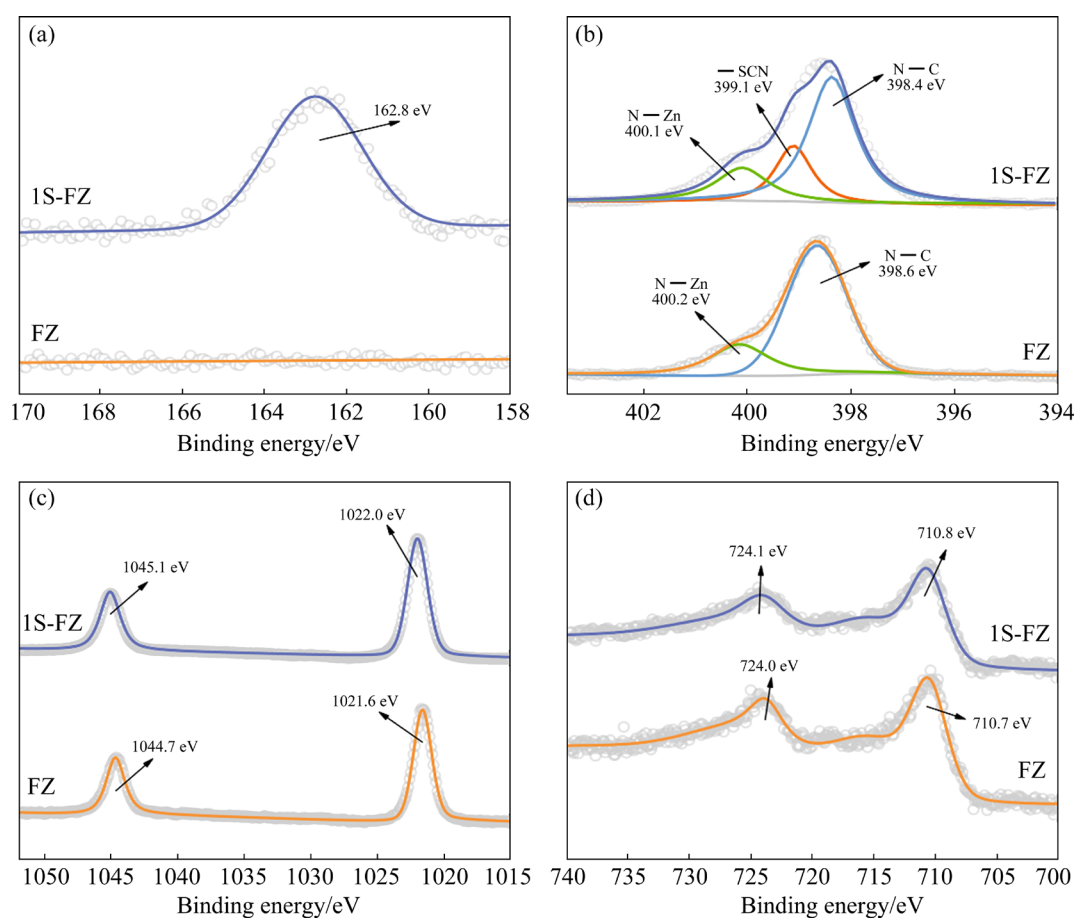
Fig. 4 XPS spectra of S 1s (a), N 1s (b), Zn 2p (c), Fe 2p (d) of FZ and 1S-FZ samples

−27.1 mV. This is mainly because ─SCN is a functional group with higher polarity and can become an electron acceptor structure resulting in the formation of an internal electric field [15].

The incorporation of ─SCN leads directly to a decrease in the crystallinity of the material. To gain further structure information, the DSC−TGA analysis was conducted. As depicted in Figs. 5(a, b), there was a mass loss during the initial heating stage (below 300 °C), primarily attributed to the removal of structural water in ZIF-L, indicating the reduction of solvent molecules in 1S-FZ [33]. This observation aligned with the FT-IR and EPR results. In comparison to FZ, 1S-FZ displayed a broader endothermic peak in the temperature range of 200−260 °C, associated with the structural transformation of low-density phase amorphous ZIF-L [34,35]. Figures 5(c, d) illustrated that the hydrophilicity of 1S-FZ was moderately enhanced compared to the FZ sample. This improvement was attributed to the introduction of certain defects through ─SCN grafting [36]. The results indicated that the enhanced hydrophilicity of the material is

primarily a consequence of the heightened surface energy of the photocatalyst induced by the increased structural defect density. The increase in hydrophilicity is advantageous for the liquid-phase photocatalytic process.

3.2 Photocatalytic performance of MOFs

Visible light constitutes 46% of natural sunlight energy. The efficiency of photocatalyst in utilizing visible light directly influences the practical viability [37]. In Fig. 6(a), the visible-light-driven photocatalytic Cr(VI) reduction performance curve without the addition of the hole scavenger is presented. For all samples, the adsorption−desorption equilibrium was ensured prior to the photocatalytic tests. The effect of photocatalyst modification on Cr(VI) adsorption was relatively minor (Table 1). The photocatalytic process of each sample conforms well to the pseudo-first-order kinetic equation, as depicted in Fig. 6(b). The fitted apparent rate constants are: 1S-FZ (0.0319 min^{-1}) > 0.5S-FZ (0.0219 min^{-1}) > FZ (0.0110 min^{-1}) > 0.2S-FZ (0.0080 min^{-1}).
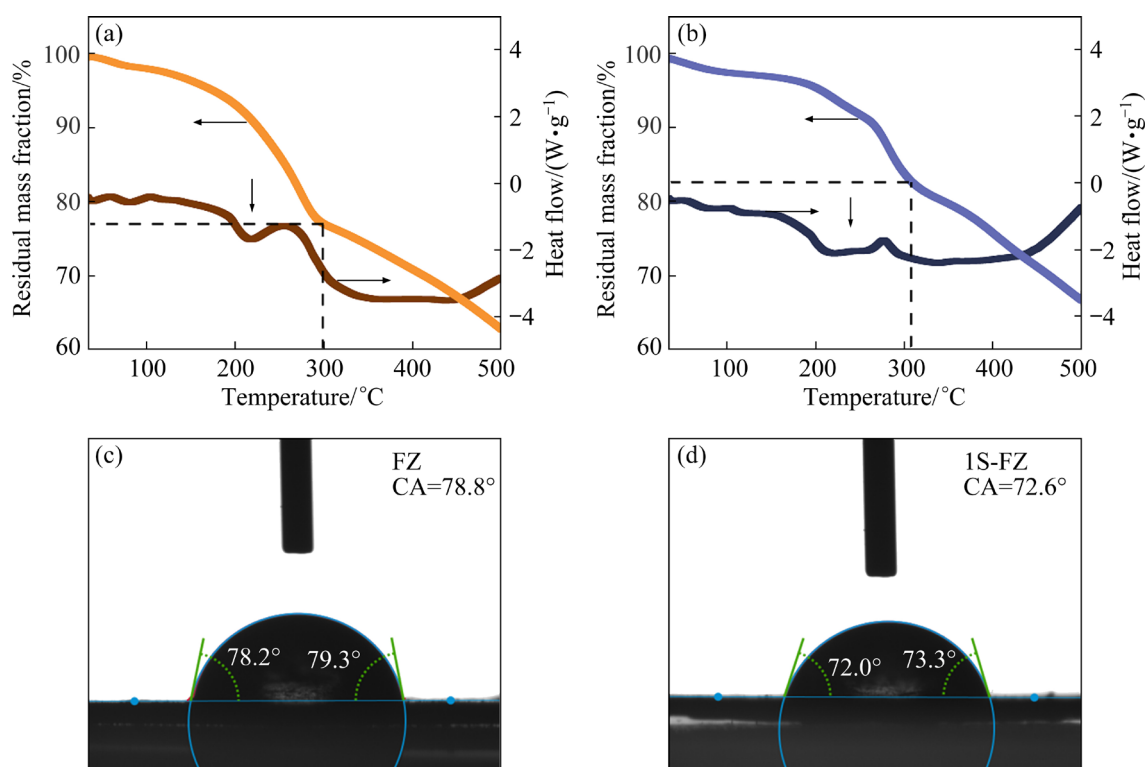
Fig. 5 DSC−TGA cruves (a, b) and water contact angle (CA) (c, d) of FZ (a, c) and 1S-FZ (b, d) samples
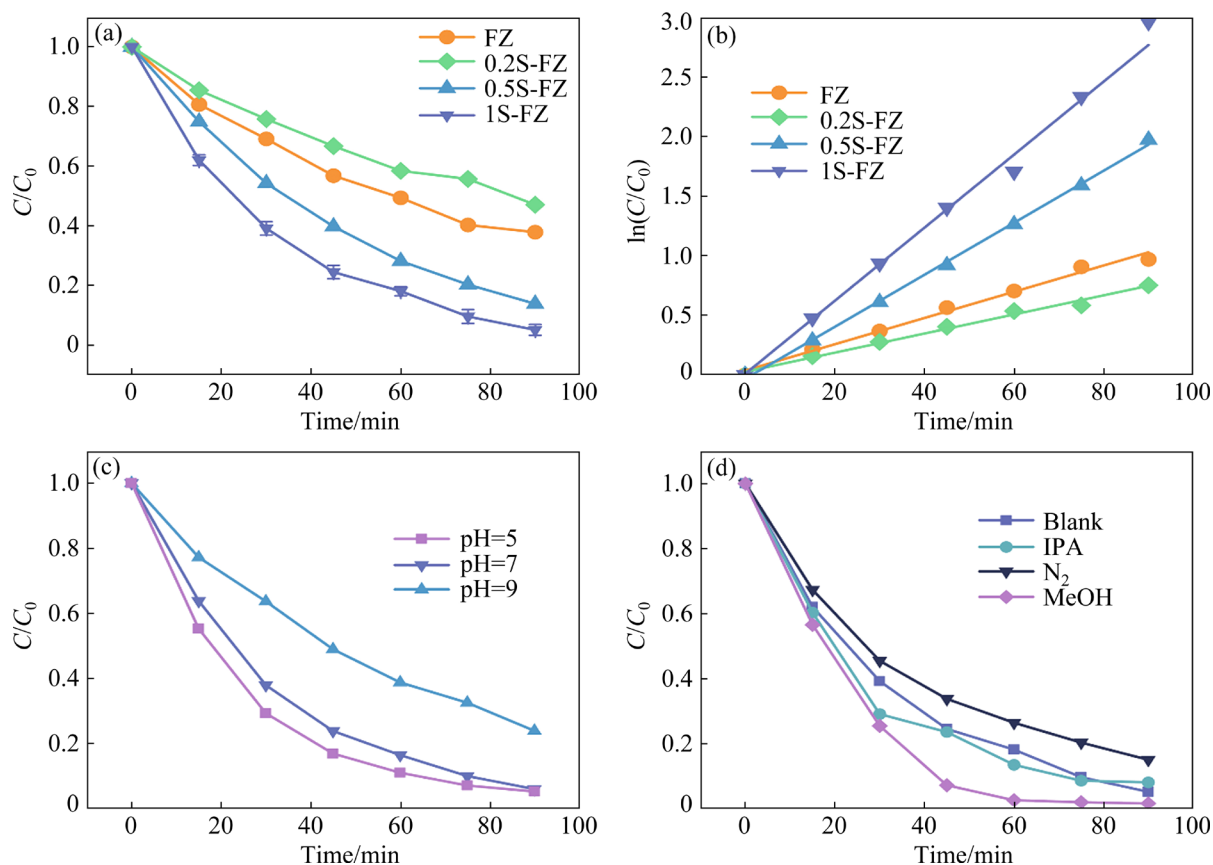
Fig. 6 Photocatalytic Cr(VI) conversion curves (a) and pseudo-first-order kinetic fitting results (b) for different samples; photocatalytic Cr(VI) conversion curves of 1S-FZ sample at different pH (c) and with different additives (d)

Specific fitting results were provided in Table 1. With the increase in KSCN addition, the performance of 0.2S-FZ slightly decreases. This is primarily attributed to the introduction of —SCN, which further enhances the negative charge on the material surface [38]. — SCN increases the repulsive force between CrO_4^{2-} ions and the MOF surface, thereby impeding the catalytic reaction. However, as the amount of —SCN replacing the original ligand continues to increase, its influence on the material's structure and charge transfer behavior becomes increasingly significant, thereby making the adverse effects on the photocatalytic activity. Both 0.5S-FZ and 1S-FZ samples exhibit improved photocatalytic performance, with the 1S-FZ sample demonstrating the highest reaction rate constant, approximately 2.8 times that of FZ. Compared with recent visible-light-driven MOFs-based photocatalytic materials, the synthesized 1S-FZ sample has relatively good activity.

Table 1 Adsorption ratio, k, and R^2 of different samples

Sample	Adsorption ratio/%	k/min^{-1}	R^2
FZ	16.4	0.0110	0.98961
0.2S-FZ	16.9	0.0080	0.99033
0.5S-FZ	19.1	0.0219	0.99863
1S-FZ	20.5	0.0307	0.99882

pH is an important factor influencing the photocatalytic reduction process of Cr(VI) [39]. By taking the optimal sample 1S-FZ as the subject of study, when pH was set to be 5, the performance of the sample was improved, with a degradation rate reaching 92.7% within 75 min. When pH is adjusted to be 9, the material's performance experiences some decline but still maintains a degradation rate of 76.0%. Compared with recent MOF photocatalysts (Table 2), 1S-FZ sample demonstrates excellent broad pH photocatalytic applicability, exhibiting good photocatalytic activity under conditions of weak acidity, neutrality, and weak alkalinity.

To identify the main active species during the photocatalyst degradation process, active species of •OH, •O$_2^-$, and h$^+$ were captured using IPA, N$_2$, and methanol, respectively [46]. After adding methanol, the catalytic activity of the material was significantly enhanced. Within 60 min, the degradation rate of 1S-FZ can reach 97.4%. It can be observed that photogenerated electrons are still the main active species in the process. The impact of •OH on the catalytic process remains minimal since the mannitol in the hybrid MOF inhibited the generation of •OH [47]. After introducing N$_2$, there is a slight decrease in the photocatalytic performance of 1S-FZ, indicating that •O$_2^-$ also

Table 2 Recent overview of visible-light-driven MOF-based photocatalysts for Cr(VI) reduction activity

| Material	Cr(VI) solution volume/mL	Concentration/ (mg·L^{-1})	Photocatalyst amount/mg	Illuminant	Time/ min	Hole scavenger	pH	Reduction efficiency/%	Resource
UiO-66-NH$_2$(Zr)	40	5	20	300 W Xe lamp (λ>400 nm)	120	–	2	98	Ref. [40]
Fe(II)-2MI	100	11.8	10	300 W Xe lamp (λ≥420 nm)	75	EDTA-2Na	4.64	~80	Ref. [41]
MIL101-(Fe)/ g-C$_3$N$_4$	40	20	20	150 W halogen lamp (λ≥420 nm)	60	Ammonium oxalate	6	67.2	Ref. [42]
Fe-BDC/ Fe-2MI	100	11.8	10	300 W Xe lamp (λ≥420 nm)	60	EDTA-2Na	4.5	100	Ref. [4]
Ru-UiO-dmbpy	40	50	10	300 W Xe lamp (λ≥420 nm)	120	Benzyl alcohol	4	65.7	Ref. [43]
Amine-functionalized ZIF-8	40	6	20	450 W Xe lamp (λ>400 nm)	180	–	8	>85	Ref. [44]
4%PDI/MIL-125(Ti)-NH$_2$	40	20	20	300 W Xe lamp (λ≥420 nm)	50	–	6	62	Ref. [45]
1S-FZ	100	30	50	300 W Xe lamp (λ≥420 nm)	90	–	7	94.8	This work

participates in the partial reduction process of Cr(VI).

3.3 Photocatalytic mechanism

The molecular orbital structure of MOFs directly determines the photocatalytic performance of the material. Fe—O clusters give ZIF-L significant light absorption activity in the visible region, which determines the basic photocatalytic ability. Compared to the FZ, the samples modified with —SCN exhibit an overall enhancement in visible light absorption intensity (Fig. 7(a)). The bandgap energy (E_g) can be calculated through Tauc formula: $(\alpha h v)^2 = A(h v - E_g)$ [48,49]. The introduction of —SCN led to the narrower E_g, primarily due to the decrease in crystallinity. The flat-band potentials of FZ and 1S-FZ were determined to be −0.53 and −0.76 V from Mott−Schottky testing (Fig. 7(c)). Considering the n-type semiconductor properties of ZIF-L, the LUMO levels of FZ and 1S-FZ were calculated to be −0.63 and −0.86 eV. Combined with the results above, schematic diagrams of the molecular orbital structures for FZ and 1S-FZ samples are depicted in Fig. 7(d). A narrower bandgap of 1S-FZ results in improved visible light responsiveness, while higher LUMO levels imply that the photogenerated electrons possess enhanced reduction activity. The HOMO energy level is higher than the water oxidation potential, so that the photogenic hole also has the ability to oxidize water molecules [50]. In addition, the XPS characteristic peaks of the Fe sites shifted significantly towards lower binding energies after the reaction, indicating an increased proportion of Fe(II) (as shown in Fig. 8). This suggests that the Fe sites in 1S-FZ, similar to those previously reported, participate in the photocatalytic process through the Fe(II)/Fe(III) redox cycle as a variable valence metal [18,51].

The photocatalytic process is caused by light-induced electron transfer, and light/electrochemical tests can be utilized to evaluate the photogenerated carrier properties of the catalysts [52,53]. As depicted in Fig. 9(a), 1S-FZ exhibited a smaller EIS radius, indicating a reduced interface charge transfer resistance [54,55]. As illustrated in Fig. 9(b), 1S-FZ demonstrated a stronger visible-light-driven transient photocurrent response, with a
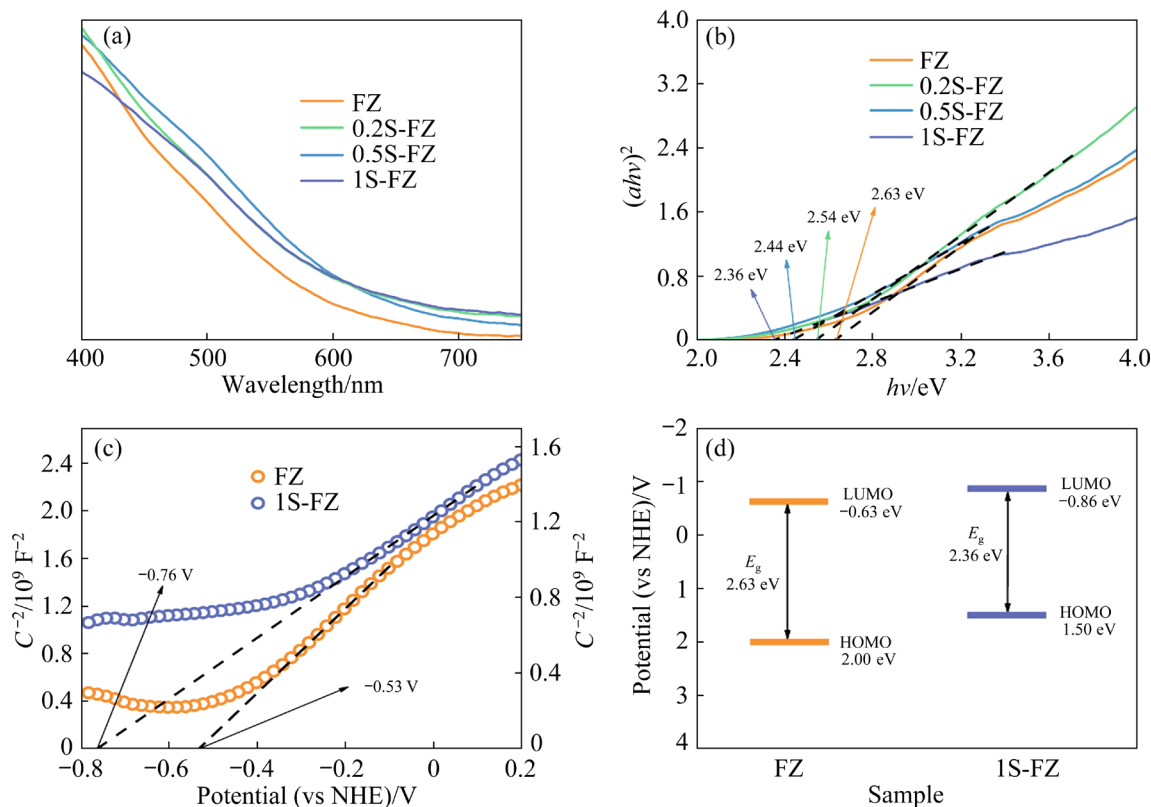
Fig. 7 DRS spectra (a), $(\alpha h v)^2$ vs $h v$ curves (b), Mott−Schottky plots (c) of FZ, 0.2S-FZ, 0.5S-FZ and 1S-FZ samples; Illustration of E_g and LUMO/HOMO levels of FZ and 1S-FZ samples (d)
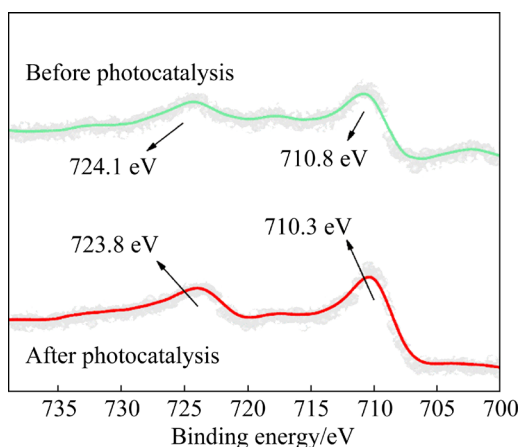
**Fig. 8** Fe 2p XPS signals of 1S-FZ sample before and after Cr(VI) reduction

current density of 0.27 μA/cm², which is 1.7 times that of the FZ sample. CV and LSV tests of the FZ and 1S-FZ samples were conducted in 0.2 mol/L neutral potassium dichromate solution, as shown in Figs. 9(c, d). Both samples exhibited prominent reduction peaks, representing the reduction process of CrO_4^{2-}/Cr^{3+} [56]. The reduction peak current of 1S-FZ is 0.240 mA/cm² at 0.125 V, which is higher than that of FZ. 1S-FZ also showed more positive potential. Furthermore, 1S-FZ demonstrated higher current density compared to FZ after illumination, consistent with the results of transient photocurrent testing [57]. In the LSV test, 1S-FZ exhibited a smaller overpotential than FZ, indicating that the introduction of —SCN facilitated rapid electron transfer to the active sites [58]. As a result, 1S-FZ exhibited a rapid charge transfer pathway with less resistance and a higher photocatalytic current density for Cr(VI) reduction under visible light.

To demonstrate the influence of —SCN on the charge carrier migration behavior, the C_{dl} values of 1S-FZ and FZ were tested, as shown in Fig. 10. The experimental results indicated a decrease in capacitance for the 1S-FZ sample compared to FZ, suggesting that —SCN effectively released electrons stored in the MOF, facilitating their participation in the photocatalytic reduction process [13,59]. The electron-withdrawing effect of
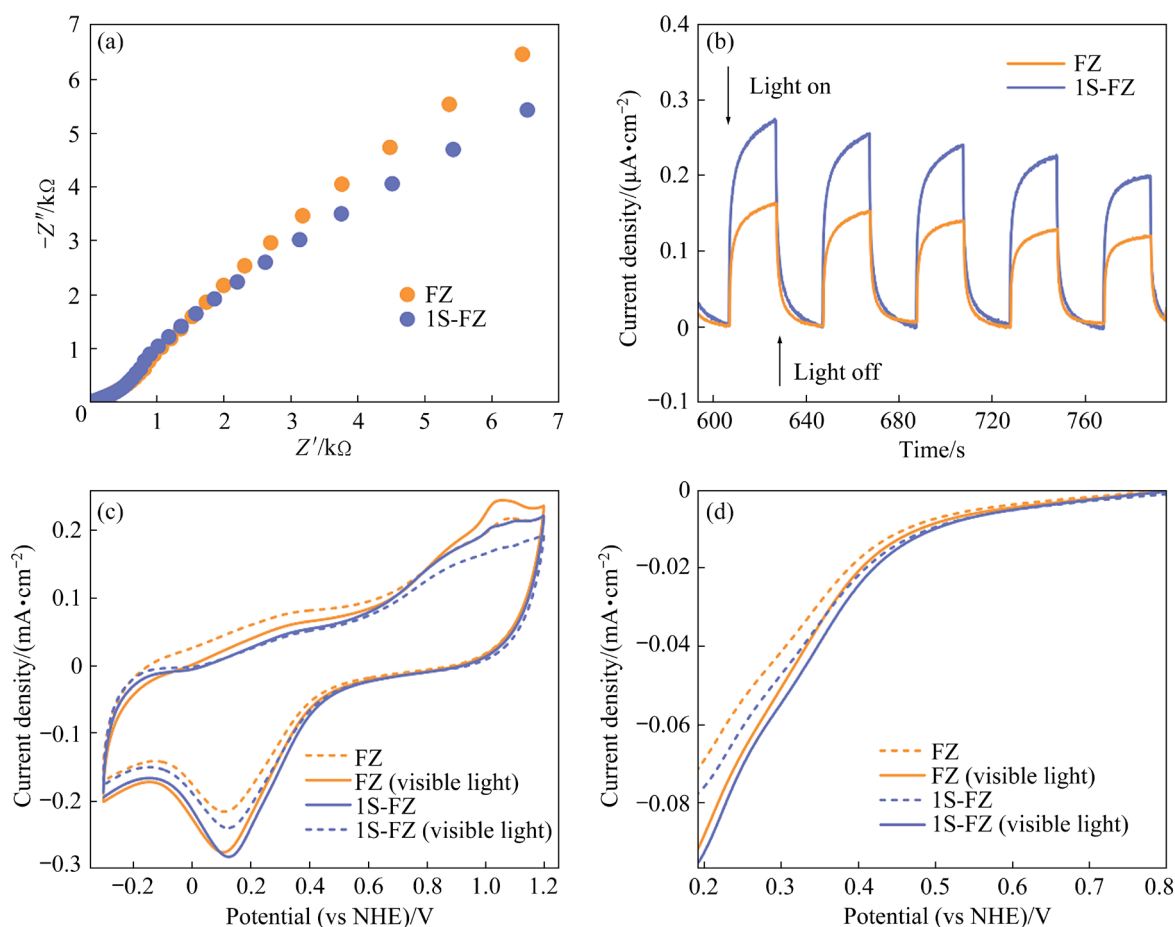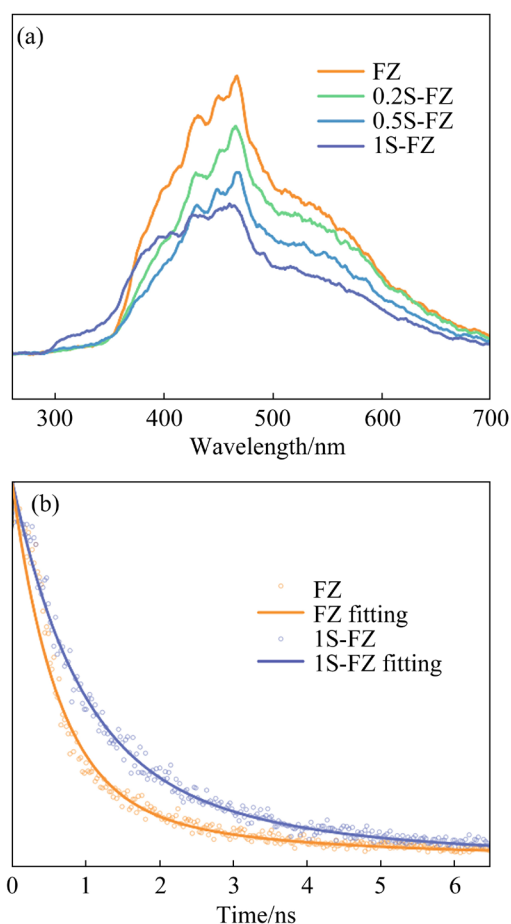

Fig. 9 EIS spectra (a), visible-light-driven current density vs time curve (b), CV curve (c) and LSV curve (d) of FZ and 1S-FZ samples
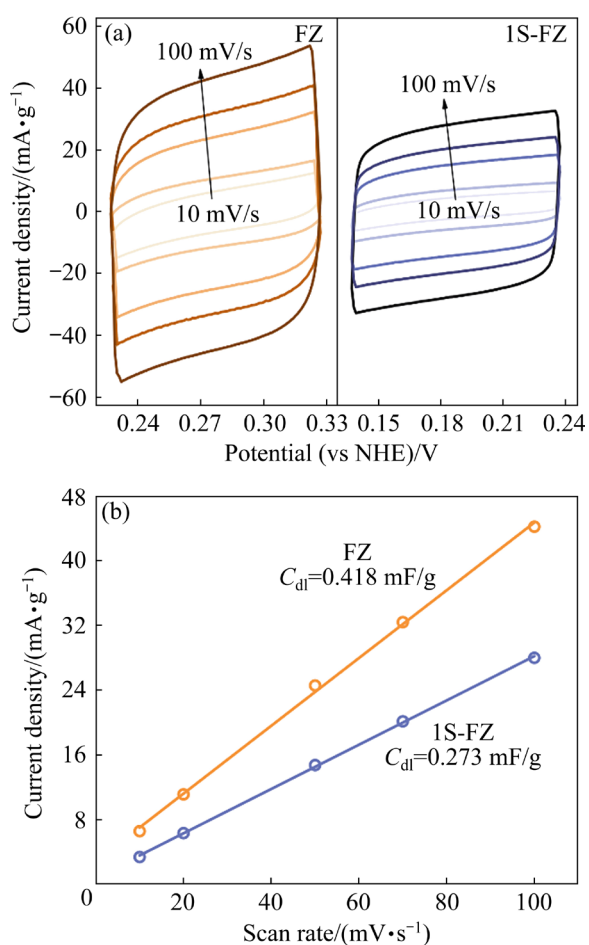
Fig. 10 CV test results at different scan rates (10, 20, 50, 70, 100 mV/s) in non-Faradaic potential range (a); C_{dl} values of FZ and 1S-FZ samples (b)

Fig. 11 PL spectra of different samples (a) and TR-PL decay curve of FZ and 1S-FZ samples (b)

Table 3 Fitting result of TR-PL decay curve of FZ and 1S-FZ at 465 nm

Sample	τ_1/ns	B_1	τ_2/ns	B_2	τ_{av}/ns
FZ	0.60	1.02	2.60	0.17	1.44
1S-FZ	0.84	0.71	2.63	0.31	1.87

The average lifetime (τ_{av}) is obtained by the equation: $\tau_{av}=(B_1\tau_1^2 + B_2\tau_2^2)/(B_1\tau_1+B_2\tau_2)$

—SCN played a significant role in regulating the charge transfer pathway [60]. Figure 11 illustrated the fluorescence performance of the samples. With the increase of —SCN content, the fluorescence intensity of the photocatalyst at 465 nm gradually decreases, indicating the restraint in the carrier recombination [61]. Additionally, due to the introduction of more structural defects and the electron-donating effect of —SCN, fluorescence lifetime of the material showed a certain enhancement (the fitting result shown in Table 3), further confirming the phenomenon of slow photocarrier recombination in the material [62].

Based on the above results, the effects of —SCN on the structure and charge transfer process of 1S-FZ sample were shown in Fig. 12. —SCN, serving as a monodentate ligand, partially replaces 2-methylimidazole. This directly led to the generation of structural defects in ZIF-L, which is the primary reason for the decrease in material crystallinity. The reduction in crystallinity lowered the bandgap energy of MOF, further enhancing the absorption of visible light. The constructed quasi-MOF structure reduced the recombination of photogenerated electron−hole pairs. The structural defects also enhance the hydrophilicity of the material by enhancing its surface energy, which is conducive to the liquid-phase catalytic process. The grafted polar functional group —SCN, due to its strong electron-withdrawing effect, facilitated charge transfer within the MOF, serving as a site for photogenerated electron release and enhancing the efficiency of charge carrier separation. The

synergistic effect of —SCN and the photosensitive component Fe—O clusters promoted visible light absorption and facilitated photogenerated electron transfer, leading to a significant enhancement in the photocatalytic activity of ZIF-L.
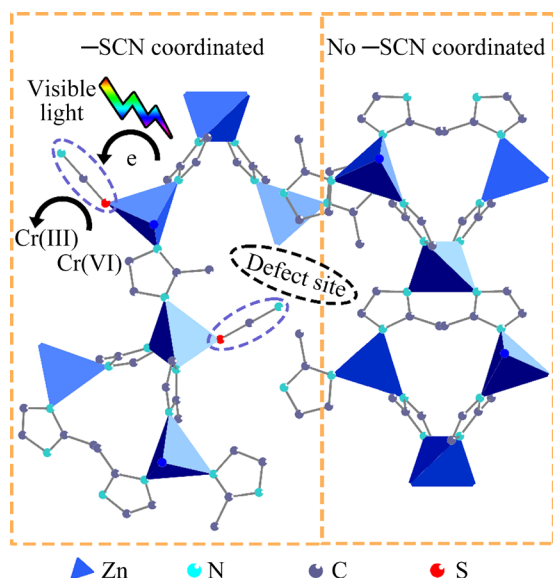
Fig. 12 Photocatalytic mechanism diagram of 1S-FZ sample

4 Conclusions

(1) A sample synthesis method of —SCN induced quasi-MOFs photocatalyst was developed. The constructed quasi-MOFs had favorable effects on the visible light response and photogenerated carrier migration.

(2) Compared to the photosensitized ZIF-L without —SCN modulation, the degradation rate and apparent rate constants for Cr(VI) of 1S-FZ sample increased from 62.1% and 0.0110 min^{-1} to 94.8% and 0.0307 min^{-1}, respectively.

(3) The introduction of —SCN partially substituted 2-methylimidazole within ZIF-L, leading to the formation of structural defects and augmenting the material's light absorption capacity. Owing to the robust electron-withdrawing capability of —SCN, an efficient electron release pathway emerged within ZIF-L, facilitating the separation of electron−hole pairs and enhancing the utilization efficiency of photogenerated electrons.

(4) Through the synergistic interplay of photosensitization and defect engineering, ZIF-L was transformed from a material lacking Cr(VI) reduction capability into a high-performance visible-light-driven photocatalyst. Considering

strong affinity of —SCN with many metal sites, this approach holds promise for applying to other MOFs.

CRediT authorship contribution statement

Declaration of competing interest

The authors declare that they have no known competing financial interests or personal relationships that could have appeared to influence the work reported in this paper.

Acknowledgments

References

[1] BAKHTIAN M, KHOSROSHAHI N, MARDANIAFZAL A, SAFARIFARD V. Enhancing photocatalytic Cr(VI) detoxification and N$_2$ fixation through construction of a Z-scheme heterojunction via partial derivatization of BiOBr on the MOF-808/Bi-BDC composite [J]. ACS Applied Engineering Materials, 2023, 1(8): 2029−2041.

[2] YOU Chang-jun, WANG Chun-chun, CAI Ming-jie, LIU Yan-ping, ZHU Bai-kang, LI Shi-jie. Improved photo-carrier transfer by an internal electric field in BiOBr/N-rich C$_3$N$_5$ 3D/2D S-scheme heterojunction for efficiently photocatalytic micropollutant removal [J]. Acta Physico-Chimica Sinica, 2024, 40: 2407014.

[3] LOFRANO G, MERIÇ S, ZENGIN G E, ORHON D. Chemical and biological treatment technologies for leather tannery chemicals and wastewaters: A review [J]. Science of the Total Environment, 2013, 461: 265−281.

[4]   HE Qin, FU Yang-jie, GE Xue-ying, AL-ENIZI A M, NAFADY A, WANG Qi, MA Sheng-qian. Facile fabrication of Fe-BDC/Fe-2MI heterojunction with boosted photo-catalytic activity for Cr(VI) reduction [J]. Journal of Environmental Chemical Engineering, 2021, 9(5): 105961.

[5]   MA Xin, DU Hao, TAN Meng, QIAN Jian-ying, DENG Man, HAO Derek, WANG Qi, ZHU Hua-yue. Photocatalytic fuel cell with cathodic P-BiVO₄/CQDs and anodic WO₃ for efficient Cr(VI) reduction and stable electricity generation [J]. Separation and Purification Technology, 2024, 339: 126644.

[6]   WANG Qi, MA Wang-gang, QIAN Jian-ying, LI Ning-yi, ZHANG Chao, DENG Man, DU Hao. S-scheme towards interfacial charge transfer between POMs and MOFs for efficient visible-light photocatalytic Cr(VI) reduction [J]. Environmental Pollution, 2024, 347: 123707.

[7]   BAGHERI M, MASOOMI M Y. Quasi-metal organic frameworks: Preparation, applications and future perspectives [J]. Coordination Chemistry Reviews, 2022, 468: 214643.

[8]   LI Shi-jie, DONG Ke-xin, CAI Ming-jie, LI Xin-yu, CHEN Xiao-bo. A plasmonic S-scheme Au/MIL-101(Fe)/BiOBr photocatalyst for efficient synchronous decontamination of Cr(VI) and norfloxacin antibiotic [J]. EScience, 2024, 4(2): 100208.

[9]   ZHUANG Chun-qiang, CHANG Yuan, LI Wei-ming, LI Shi-jie, XU Peng, ZHANG Hang, ZHANG Yi-hong, ZHANG Can, GAO Jun-feng, CHEN Ge, ZHANG Tian-yang, KANG Zhen-hui, HAN Xiao-dong. Light-induced variation of lithium coordination environment in g-C₃N₄ nanosheet for highly efficient oxygen reduction reactions [J]. ACS Nano, 2024, 18(6): 5206−5217.

[10]   WU Shuai, YU Hong-tao, CHEN Shuo, QUAN Xie. Enhanced photocatalytic H₂O₂ production over carbon nitride by doping and defect engineering [J]. ACS Catalysis, 2020, 10(24): 14380−14389.

[11]   LUO Dan, LI Chao-jie, ZHANG Yong-guang, MA Qian-yi, MA Chu-yin, NIE Yi-hang, LI Matthew, WENG Xue-fei, HUANG Rong, ZHAO Yan, SHUI Ling-ling, WANG Xin, CHEN Zhong-wei. Design of quasi-MOF nanospheres as a dynamic electrocatalyst toward accelerated sulfur reduction reaction for high-performance lithium−sulfur batteries [J]. Advanced Materials, 2022, 34(2): 2105541.

[12]   ZHANG Li, GUO Yuan, GUO Chang-yan, CHEN Ting-xiang, FENG Chao, QIAO Shan-shan, WANG Ji-de. Construction of defective zeolitic imidazolate frameworks with improved photocatalytic performance via vanillin as modulator [J]. Chemical Engineering Journal, 2021, 421: 127839.

[13]   WANG Ping, SHENG Yue, WANG Fa-zhou, YU Huo-gen. Synergistic effect of electron-transfer mediator and interfacial catalytic active-site for the enhanced H₂-evolution performance: A case study of CdS−Au photocatalyst [J]. Applied Catalysis B: Environmental, 2018, 220: 561−569.

[14]   ZHANG Li-na, LIU Tong-ling, LIU Tai-feng, HUSSAIN S, LI Qiu-ye, YANG Jian-jun. Improving photocatalytic performance of defective titania for carbon dioxide photoreduction by Cu cocatalyst with SCN⁻ ion modification [J]. Chemical Engineering Journal, 2023, 463: 142358.

[15]   FU Fang-yu, SHOWN I, LI Chia-shuo, RAGHUNATH P, LIN Tsai-Yu, BILLO T, WU Heng-liang, WU C I, CHUNG Po-wen, LIN Ming-chang, CHEN Li-Chyong, CHEN Kuei-Hsien. KSCN-induced interfacial dipole in black TiO₂

[16]   WANG Tsai-Te, CHIANG Chao-Lung, LIN Yu-Chang, SRINIVASADESIKAN V, LIN Ming-chang, LIN Yan-gu. KSCN-activation of hydrogenated NiO/TiO₂ for enhanced photocatalytic hydrogen evolution [J]. Applied Surface Science, 2020, 511: 145548.

[17]   FENG Yi, CHEN Qian, CAO Meng-jue, LING Nan, YAO Jian-feng. Defect-tailoring and titanium substitution in metal-organic framework UiO-66-NH₂ for the photocatalytic degradation of Cr(VI) to Cr(III) [J]. ACS Applied Nano Materials, 2019, 2(9): 5973−5980.

[18]   ZHANG Yi, TAN Peng-fei, YANG Lu, ZHANG Shao-hui, ZHOU Bin-hua, ZHANG Xiao-qing, HUANG Hong-jun, PAN Jun. Mannitol-assisted Fe-O clusters@ZIF-L for Cr(VI) photocatalytic reduction under neutral conditions inspired by Fe-based MOFs photocatalysts [J]. Separation and Purification Technology, 2023, 320: 124174.

[19]   CHENG Cheng, MAO Liu-hao, KANG Xing, DONG Chung-li, HUANG Yu-cheng, SHEN Shao-hua, SHI Jin-wen, GUO Lie-jin. A high-cyano groups-content amorphous-crystalline carbon nitride isotype heterojunction photocatalyst for high-quantum-yield H₂ production and enhanced CO₂ reduction [J]. Applied Catalysis B: Environmental, 2023, 331: 122733.

[20]   LIU Guan-hua, JIANG Zhong-yi, CAO Ke-teng, NAIR San-kar, CHENG Xuan-xuan, ZHAO Jing, GOMAA H, WU Hong, PAN Fu-sheng. Pervaporation performance comparison of hybrid membranes filled with two-dimensional ZIF-L nanosheets and zero-dimensional ZIF-8 nanoparticles [J]. Journal of Membrane Science, 2017, 523: 185−196.

[21]   ULLAH S, BUSTAM M A, AL-SEHEMI A G, ASSIRI M A, GONFA G, MUKHTAR A, AYOUB M, AHMAD T. Experimental investigations on the regeneration of desulfurized 1-butyl-3-methylimidazolium tetrachloroferrate [Bmim][FeCl₄] and 1-butyl-3-methylimidazolium thiocyanate [Bmim][SCN] ionic liquids: A raman spectroscopic study [J]. Journal of Raman Spectroscopy, 2020, 51(3): 546−554.

[22]   GAO Yuan-hao, WU Jie-ying, LI Yi-ming, SUN Ping-ping, ZHOU Hong-ping, YANG Jia-xiang, ZHANG Sheng-yi, JIN Bao-kang, TIAN Yu-peng. A sulfur-terminal Zn(II) complex and its two-photon microscopy biological imaging application [J]. Journal of the American Chemical Society, 2009, 131(14): 5208−5213.

[23]   KUMARI G, JAYARAMULU K, MAJI T K, NARAYANA C. Temperature induced structural transformations and gas adsorption in the zeolitic imidazolate framework ZIF-8: A Raman study [J]. Journal of Physical Chemistry A, 2013, 117(43): 11006−11012.

[24]   LIU Shou-qing, XIAO Bo, FENG Lian-rong, ZHOU Shan-shan, CHEN Zhi-gang, LIU Cheng-bao, CHEN Feng, WU Zheng-ying, XU Nan, OH Won-Chun, MENG Ze-da. Graphene oxide enhances the Fenton-like photocatalytic activity of nickel ferrite for degradation of dyes under visible light irradiation [J]. Carbon, 2013, 64: 197−206.

[25]   GAO Yuan-hao, ZHANG Xiao-fei, WANG Pei-pei, LEI Yan, YANG Xiaognag, FA Wen-jun, NIU He-lin, ZHENG Zhi. A novel π-conjugated Zn←S→Zn unit interface in the ZnS/Zn(S)₂L inorganic/orgainc hybrids for significant photoelectric response [J]. Applied Surface Science, 2017,

402: 336−343.

[26] NASIR A M, NORDIN NAH Md, GOH P S, ISMAIL A F. Application of two-dimensional leaf-shaped zeolitic imidazolate framework (2D ZIF-L) as arsenite adsorbent: Kinetic, isotherm and mechanism [J]. Journal of Molecular Liquids, 2018, 250: 269−277.

[27] DING Bing, WANG Xian-biao, XU Yong-fei, FENG Shao-jie, DING Yi, PAN Yang, XU Wei-fan, WANG Huan-ting. Hydrothermal preparation of hierarchical ZIF-L nanostructures for enhanced CO_2 capture [J]. Journal of Colloid and Interface Science, 2018, 519: 38−43.

[28] YUAN Shu-shan, ZHU Jun-yong, LI Yi, ZHAO Yan, LI Jian, van PUYVELDE P, van der BRUGGEN B. Structure architecture of micro/nanoscale ZIF-L on a 3D printed membrane for a superhydrophobic and underwater superoleophobic surface [J]. Journal of Materials Chemistry A, 2019, 7(6): 2723−2729.

[29] SONG Ming-ming, SONG Xiang-hai, LIU Xin, ZHOU Wei-qiang, HUO Peng-wei. Enhancing photocatalytic CO_2 reduction activity of $ZnIn_2S_4$/MOF-808 microsphere with S-scheme heterojunction by in situ synthesis method [J]. Chinese Journal of Catalysis, 2023, 51: 180−192.

[30] XIE Chi-peng, HU Xiu-li, GUAN Zhao-yong, LI Xiao-dong, ZHAO Fu-hua, SONG Yu-wei, LI Yuan, LI Xiao-fang, WANG Ning, HUANG Chang-shui. Tuning the properties of graphdiyne by introducing electron-withdrawing/donating groups [J]. Angewandte Chemie, 2020, 132(32): 13644−13648.

[31] CAI Ming-jie, LIU Yan-ping, DONG Ke-xin, CHEN Xiao-bo, LI Shi-jie. Floatable S-scheme Bi_2WO_6/C_3N_4/carbon fiber cloth composite photocatalyst for efficient water decontamination [J]. Chinese Journal of Catalysis, 2023, 52: 239−251.

[32] LI Shi-jie, CAI Ming-jie, WANG Chun-chun, LIU Yan-ping. Ta_3N_5/CdS core–shell S-scheme heterojunction nanofibers for efficient photocatalytic removal of antibiotic tetracycline and Cr(VI): Performance and mechanism insights [J]. Advanced Fiber Materials, 2023, 5(3): 994−1007.

[33] ŞAHIN F, TOPUZ B, KALıPçıLAR H. Synthesis of ZIF-7, ZIF-8, ZIF-67 and ZIF-L from recycled mother liquors [J]. Microporous and Mesoporous Materials, 2018, 261: 259−267.

[34] YANG Fan, LI Wei-yang, TANG Bohe-jin. Facile synthesis of amorphous UiO-66 (Zr−MOF) for supercapacitor application [J]. Journal of Alloys and Compounds, 2018, 733: 8−14.

[35] WANG Qi, CHEN Mei-mei, ZHU Na-xin, SHI Xiao-dong, JIN Huan, ZHANG Yi, CONG Yan-qing. Preparation of AgI sensitized amorphous TiO_2 as novel high-performance photocatalyst for environmental applications [J]. Journal of Colloid and Interface Science, 2015, 448: 407−416.

[36] KWOK D Y, NEUMANN A W. Contact angle interpretation in terms of solid surface tension [J]. Colloids and Surfaces A: Physicochemical and Engineering Aspects, 2000, 161(1): 31−48.

[37] HE Xiao-die, HE Ti-wei, XIA Rui-di, QI Yu-fan, ZHOU Yun-jie, SONG Bin, LIAO Fan, KANG Zhen-hui, JIANG Lin. SnS_2/SnS heterojunction: An all-weather-active photocatalyst for Cr(VI) removal [J]. Separation and Purification Technology, 2023, 324: 124515.

[38] YOON Jaekyung, SHIM Eunjung, BAE Sanghyun, JOO Hyunku. Application of immobilized nanotubular TiO_2 electrode for photocatalytic hydrogen evolution: Reduction of hexavalent chromium (Cr(VI)) in water [J]. Journal of Hazardous Materials, 2009, 161(2/3): 1069−1074.

[39] WANG Chong-Chen, REN Xue-ying, WANG Peng, CHANG Cheng. The state of the art review on photocatalytic Cr(VI) reduction over MOFs-based photocatalysts: From batch experiment to continuous operation [J]. Chemosphere, 2022, 303: 134949.

[40] DU Xue-dong, YI Xiao-hong, WANG Peng, ZHENG Wei-wei, DENG Ji-guang, WANG Chong-chen. Robust photocatalytic reduction of Cr (VI) on UiO-66-NH_2 (Zr/Hf) metal-organic framework membrane under sunlight irradiation [J]. Chemical Engineering Journal, 2019, 356: 393−399.

[41] GAO Qiao-yuan, LIN Da-gang, FAN Yong-jie, HE Qin, WANG Qi. Visible light induced photocatalytic reduction of Cr(VI) by self-assembled and amorphous Fe-2MI [J]. Chemical Engineering Journal, 2019, 374: 10−19.

[42] ZHAO Fei-ping, LIU Yong-peng, HAMMOUDA S B, DOSHI B, GUIJARRO N, MIN Xiao-bo, TANG Chong-jian, SILLANPÄÄ M, SIVULA K, WANG Shao-bin. MIL-101(Fe)/g-C_3N_4 for enhanced visible-light-driven photocatalysis toward simultaneous reduction of Cr(VI) and oxidation of bisphenol A in aqueous media [J]. Applied Catalysis B: Environmental, 2020, 272: 119033.

[43] ZHENG He-qi, HE Xing-hao, ZENG Yong-nian, QIU Wei-hua, CHEN Jin, CAO Gao-juan, LIN Rong-guang, LIN Zu-jin, CHEN Bang-lin. Boosting the photoreduction activity of Cr(VI) in metal-organic frameworks by photosensitiser incorporation and framework ionization [J]. Journal of Materials Chemistry A, 2020, 8(33): 17219−17228.

[44] HU Chechia, HUANG Yu-chi, CHANG Ai-lun, NOMURA M. Amine functionalized ZIF-8 as a visible-light-driven photocatalyst for Cr(VI) reduction [J]. Journal of Colloid and Interface Science, 2019, 553: 372−381.

[45] WANG Shi-hui, XIA Yu-zhou, YAN Gui-yang, CHEN Mei-xia, WANG Xu-xu, WU Ling, LIANG Ruo-wen. PDI bridged MIL-125(Ti)-NH_2 heterojunction with frustrated Lewis pairs: A promising photocatalyst for Cr(VI) reduction and antibacterial application [J]. Applied Catalysis B: Environmental, 2022, 317: 121798.

[46] LI Shi-jie, CAI Ming-jie, LIU Yan-ping, WANG Chun-chun, YAN Ru-yu, CHEN Xiao-bo. Constructing $Cd_{0.5}Zn_{0.5}S$/Bi_2WO_6 S-scheme heterojunction for boosted photocatalytic antibiotic oxidation and Cr(VI) reduction [J]. Advanced Powder Materials, 2023, 2(1): 100073.

[47] LU Si-min, ZHANG Xiao, CHEN Ling, YANG Ping. Colorimetric visualization of superoxide dismutase in serum via etching of Au nanorods from superoxide radical [J]. Sensors and Actuators B: Chemical, 2018, 259: 1066−1072.

[48] TAUC J, MENTH A. States in the gap [J]. Journal of Non-Crystalline Solids, 1972, 8: 569−585.

[49] SCHUKRAFT G EM, MOSS B, KAFIZAS A G, PETIT C. Effect of band bending in photoactive MOF-based heterojunctions [J]. ACS Applied Materials & Interfaces, 2022, 14(17): 19342−19352.

[50] XIA Jia-hui, TIAN Jing-zhuo, SUN Tao, FAN Jun, LIU En-zhou. Conductive $Co_{1.5}MoS_{3.2}$ promoted photocatalytic H_2 production over g-C_3N_4 [J]. Surfaces and Interfaces, 2024, 47: 104218.

[51] GUO Jia-ying, ZHOU Yu-fei, YU Ming-chuan, LIANG Huan-jing, NIU Jun-feng. Construction of Fe^{2+}/Fe^{3+} cycle

system at dual-defective carbon nitride interfaces for photogenerated electron utilization [J]. Separation and Purification Technology, 2022, 285: 120357.

[52] BAKHTIARNIA S, SHEIBANI S, BILLARD A, AUBRY E, YAZDI M A P. Deposition of nanoporous BiVO₄ thin-film photocatalyst by reactive magnetron sputtering: Effect of total pressure and substrate [J]. Transactions of Nonferrous Metals Society of China, 2022, 32(3): 957−971.

[53] XIE Fang-xia, ZHANG Lu-lu, ZHANG Xiao, ZHANG Mei, XUAN JIAN, LIU Jian-xin, ZHANG Xiao-chao, WANG Ya-wen, RUI LI, FAN Cai-mei. Enhancement of visible light photocatalytic pharmaceutical degradation and hydrogen evolution of Bi₅O₇Br by in situ disorder engineering [J]. Transactions of Nonferrous Metals Society of China, 2023, 33(6): 1862−1872.

[54] CONG Yan-qing, ZHANG Shi-yi, ZHENG Qiuang, LI Xin-yue, ZHANG Yi, LV Shi-wen. Oxygen-modified graphitic carbon nitride with nitrogen-defect for metal-free visible light photocatalytic H₂O₂ evolution [J]. Journal of Colloid and Interface Science, 2023, 650: 1013−1021.

[55] ZENG Wei-xuan, BIAN Yuan, CAO Sheng, ZHU An-quan, QIAO Lu-lu, MA Yong-jin, TAN Peng-fei, MA Quan-yin, DONG Rui, PAN Jun. Construction of two dimensional Sr₂Ta₂O₇/S-doped g-C₃N₄ nanocomposites with Pt cocatalyst for enhanced visible light photocatalytic performance [J]. Applied Surface Science, 2019, 478: 334−340.

[56] YI J M, KIM T J, PARK S J, HONG Sung-min, KANG J G, RHEE C K, KIM J, SOHN Y K. Photoelectrochemical and photocatalytic detoxification of Cr(VI) to Cr(III) over terpyridine-derivatized Au nanoparticles on carbon paper and indium−tin-oxide electrodes [J]. Chemical Engineering Journal, 2020, 402: 126266.

[57] WENG Bo, LU Kang-qiang, TANG Zi-chao, CHEN Hao-ming, XU Yi-jun. Stabilizing ultrasmall Au clusters for enhanced photoredox catalysis [J]. Nature Communications, 2018, 9(1): 1543.

[58] SHAN Lian-wei, FANG Zi-lan, DING Guo-dao, SHI Zi-qi, DONG Li-min, LI Dan, WU Hai-tao, LI Xue-jiao, SURIYAPRAKASH J, ZHOU Yang-tao, XIAO Yan-wei. Electron confinement promoted the electric double layer effect of BiOI/β-Bi₂O₃ in photocatalytic water splitting [J]. Journal of Colloid and Interface Science, 2024, 653: 94−107.

[59] SHEN Yu-ke, LI De-kang, DANG Yu-ying, ZHANG Jia-wei, WANG Wei, MA Bao-jun. A ternary calabash model photocatalyst (Pd/MoP)/CdS for enhancing H₂ evolution under visible light irradiation [J]. Applied Surface Science, 2021, 564: 150432.

[60] LUO Li, LI De-kang, DANG Yu-ying, WANG Wei, YU Guang-suo, LI Jin, MA Bao-jun. Capacitance catalysis: Positive and negative effects of capacitance of Mo₂C in photocatalytic H₂ evolution [J]. ACS Sustainable Chemistry & Engineering, 2022, 10(18): 5949−5957.

[61] LIU Wen-wen, SHANG Yan-yang, ZHU An-quan, TAN Peng-fei, LIU Yi, QIAO Lu-lu, CHU De-wei, XIONG Xiang, PAN Jun. Enhanced performance of doped BiOCl nanoplates for photocatalysis: Understanding from doping insight into improved spatial carrier separation [J]. Journal of Materials Chemistry A, 2017, 5(24): 12542−12549.

[62] ZENG Wei-xuan, BIAN Yuan, CAO Sheng, MA Yong-jin, LIU Yi, ZHU An-quan, TAN Peng-fei, PAN Jun. Phase transformation synthesis of strontium tantalum oxynitride-based heterojunction for improved visible light-driven hydrogen evolution [J]. ACS Applied Materials & Interfaces, 2018, 10(25): 21328−21334.

硫氰基改性准 MOF 光催化剂用于增强中性条件下六价铬的可见光还原

张 翼 [1]，廖寒潇 [2]，杨 璐 [3]，周斌华 [1]，刘烜志 [1]，
翟欢欢 [1]，何晓荣 [1]，黄红军 [4]，谭鹏飞 [1]，潘 军 [1]

1. 中南大学 粉末冶金国家重点实验室，长沙 410083；
2. 中南大学 冶金与环境学院，长沙 410083；
3. 长沙学院 环境光催化应用技术湖南省重点实验室，长沙 410022；
4. 中南大学 资源加工与生物工程学院，长沙 410083

摘 要：为了解决六价铬的光催化还原常常受到光催化剂中电子利用效率不高的问题，开发了一种使用硫氰酸基 (—SCN)作为调节剂合成的准金属有机框架光催化剂，以增强光催化剂的电荷转移特性。—SCN 引入结构缺陷，改善可见光吸收和光生电子的还原能力。—SCN 显著调整电子特性，并建立稳定的电子释放路径，充当还原的活性位点。在中性硫氰酸钾溶液中，优化后的光催化剂在可见光下无需添加空穴捕获剂就能实现 94.8%的 Cr(VI)还原率。反应速率常数是未经缺陷化处理的光催化剂的 2.8 倍。这项研究提供了一种用于开发环境修复的高效光催化剂的有效策略。

关键词：准 MOF；极性官能团；光催化；六价铬还原

(Edited by Bing YANG)